GROUND DEFORMATION ASSESSMENT OF THE ALBERTINE GRABEN USING INSAR

J.R. Otukei [a], P.Atolerea[b], A.Gidudu[a], F.Martini[c]

[a] Department of Geomatics and Land Management, Makerere University, Kampala-Uganda, jrotukei@cedat.mak.ac.ug
[b] Department of Civil and Environmental Engineering, Makerere University, Kampala-Uganda
[c] Tullow Geophysical Group, Dublin

DOI: *http://dx.doi.org/10.4314/sajg.v8i2.2*

Abstract

Information on deformation of the land surface is vital for planning of infrastructure especially in areas such as the Albertine graben with substantial amounts of oil discoveries. Traditionally, global positioning systems, precise leveling and geotechnical techniques have been used for assessing and monitoring ground deformations. While these techniques provide accurate information, they are point based, expensive, time consuming and labour intensive over large area monitoring. This study explored an interferometric synthetic aperture radar (InSAR) approach for mapping deformation over Buliisa oil discovery area located in the Western arm of the East African rift valley. The method was implemented by measuring the phase differences of ALOS PALSAR data acquired between 2007 and 2011. Deformation estimates varied between -0.45m to +0.34m while the mean displacements varied from –0.10m to 0.089m. High ground deformation was detected in the Southern, North Eastern and North Western parts contributed by agricultural activity and drilling pad constructions. Generally, analysis of ALOS PALSAR data using InSAR approach provides a viable option for assessing land surface deformation in Buliisa oil exploration area.

Keywords: *Deformation, INSAR, differential interferometry*

1. Introduction

The deformation of the earth's surface is one of the prominent phenomena associated with earthquakes, land subsidence, volcanic eruptions and anthropogenic processes (Bürgmann, Rosen, & Fielding, 2000; Fujiwara et al., 2017; Gabriel, Goldstein, & Zebker, 1989; Jo, Jung, & Yun, 2017; Kang, Zhao, Zhang, Lu, & Li, 2017). Information on deformation of the land surface is vital for planning of infrastructure especially in areas such as the Albertine graben-western Uganda, with substantial amounts of oil discoveries and prone to earthquakes. The Albertine region is arguably the most seismically active area in Uganda as well as the east African region (Maasha, 1975; V. Midzi et al., 1999). Figure 1 shows reported earthquake events in eastern African countries that occurred between 2000 and 2017.

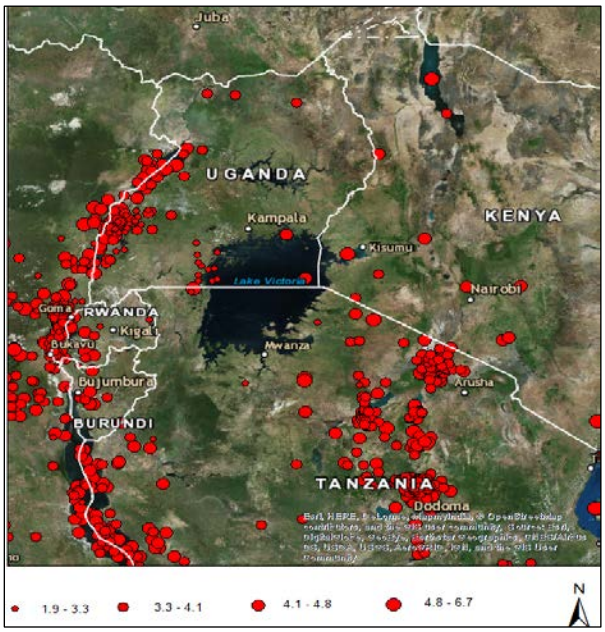

Figure 1: Earthquake events east African countries with magnitudes ranging from 0 and 10

It is evident that the western rift valley spanning through lakes Kyoga and Tanganyika has the most earthquake occurrences. Monitoring ground deformations continuously through precise mapping provides an opportunity to understand the earth dynamics in relationship to tectonic, seismic and volcanic activity (Bakon, Papco, Perissin, Sousa, & Lazecky, 2016; Braunmüller & Orosz, 2012; Henderson & Lewis, 1998; Ruiz-Armenteros et al., 2016). This ultimately helps in providing early warning mechanism in areas susceptible to ground deformations. Traditionally, global positioning systems, tilt meter, inclinometer, shape acceleration array, precise leveling and geotechnical techniques have been used for estimating and monitoring ground deformations (Bakon et al., 2016; Fumiaki et al., 2004; Lagios et al., 2013; Meilano, Fumiaki, Kazuro, Takeshi, & Atsushi, 2004). Although these methods provide accurate and reliable results, they are expensive and time consuming for large area monitoring. This is mainly due to the need to have high point density and frequency of measurement over time which is difficult to implement.

The development of light detection and ranging (LiDAR) technology has improved deformation monitoring using point based measurements over large areas due to its ability to generate high amounts of point clouds required for generating highly accurate digital terrain models. Such terrain models serve as a basis for deformation monitoring. Unfortunately, LiDAR surveys are done infrequently and often commissioned if reasonable information is available regarding existing deformation in a given area.

Interferometric synthetic aperture radar (InSAR) technique based on earth orbiting satellites provides a new tool for deformation monitoring with the capability of measuring dense points in an accurate,

efficient and cost effective manner (Bakon et al., 2016; Braunmüller & Orosz, 2012; Bürgmann et al., 2000; Carrasco, Alonso, & Broquetas, 1995; Jing-xiang & Hong, 2009; Jo et al., 2017; Ruiz-Armenteros et al., 2016). This requires derivation of interferometric phase using master and slave complex synthetic aperture radar (SAR) images and utilizing the result for generating three dimensional or displacement images (van Genderen, 1996; Xiaobing , Ni-Bin , & Shusun 2009). However, the success of InSAR requires among other considerations, a minimum of two coherent SAR images of the same portion of the earth's surface acquired from either single or repeat pass interferometry. The interferometric phase is derived by multiplying the complex SAR image of master antennae with complex conjugate of the SAR image of the slave antennae (Mather, 2004).

Space-borne satellites such as ALOS PALSAR, ERS, Sentinel-1A, ENVISAT ASAR, TerraSAR-X, Radarsat-2 (Bakon et al., 2016; Barra et al., 2016; Jing-xiang & Hong, 2009), provide SAR images which can be analyzed to provide accurate small displacements measurements over wide areas without the need for in situ observations (Bakon et al., 2016). Applications of radar interferometry for geophysical studies gained momentum in 1990s (Massonnet & Feigl, 1998; Massonnet et al., 1993; van Genderen, 1996) and research is still ongoing in this field (Bakon et al., 2016; Fujiwara et al., 2017; Imamoglu, Kahraman, Cakir, & Sanli, 2019; Liu et al., 2013; Ruiz-Armenteros et al., 2016; Schlögel, Doubre, Malet, & Masson, 2015a; Sun et al., 2015).

While InSAR technique has been successfully applied for landslide detection, deformation mapping and vegetation mapping in many parts of the world (Bakon et al., 2016; Barra et al., 2016; Jing-xiang & Hong, 2009; Liu et al., 2013; Novellino et al., 2017; Schlögel, Doubre, Malet, & Masson, 2015b; Sun et al., 2015), Uganda is yet to fully utilize this technology for addressing human and environmental challenges. The overall aim of this study was to assess the land surface deformation in Bullisa oil discovery in western Uganda using ALOS PALSAR data acquired between 2007 and 2011. The ALOS PALSAR data has shown potential for deformation monitoring with displacement estimate consistent with ground based measurements (Schlögel et al., 2015a). The long wavelength used by ALOS PALSAR satellite provides high interferometric coherence images suitable for deformation monitoring caused by earthquakes, landslides, oil pumping, land cover changes and land subsidence (Shimada & Miyagi, 2009). The area was selected because of the recent oil discoveries as well as the heightened seismic activity given the number of earthquake events recorded over the years (V. Midzi, Hlatywayo, D., Chapola, L., Kebede, F., Atakan, K., Lombe, D., Turyomurugyendo, G., & Tugume, F, 1999).

2. Study area

The study area is located in Buliisa district bounded by the geographic co-ordinates: (0.5^0 -4.0^0) N and (29.5^0-32^0) E. It comprises of Kigogole, Ngege, Wairindi, Kasemene, Nsoga and Ngara oil wells as well as parts of the western rift valley region. Generally, the area is rural with subsistence farming, fishing and cattle raring as the main economic activities. Despite the fact that the district has a low population

density compared to the national average, over 93% of the its population lives in the rural areas (UBOS, 2014). The high number of earthquakes recorded over the years suggests that the area has a high seismic and tectonic activity. Additionally, the recent discoveries of oil deposit and drilling leads to ground deformation. Related studies have demonstrated the relationship between ground subsidence and oil drilling (Lubitz, Motagh, & Kaufmann, 2014; Zhang, Lu, & Kim, 2018). It is on this basis that the area was selected for deformation analysis using ALOS PALSAR data.

3. Data and methods

3.1. Data

A total of 9 raw ALOS PALSAR images covering the period January 2007 to March 2011 with spatial resolution of 10 m by 10 m and scene size of 70 km by 70 km (Shimada, 2010) were used for deformation analysis. The images were acquired in ascending pass with an off nadir angle of 34.3^{o} and located on row 3 and path 620. Table 1 shows additional information of the SAR data used for the study. For deformation analysis, the SAR data was divided into three intervals: February 2007 until October 2007, August 2008 to October 2009 and October 2010 up to March 2011. This was done to provide deformation patterns on approximately yearly basis.

3.2. Data processing

3.2.1. Interferometric pairs

Data processing for deformation analysis requires a priori selection of interferometric SAR data pairs. One of the images is designated *a master* while the second as *a slave*. The following criteria was used for data selection: 1) a shorter perpendicular baseline and longer temporal baseline for ground deformation analysis. The perpendicular and temporal baselines were calculated with reference to the master images for each time interval, 2) one pair with 46 days temporal separation was used as topographic reference and 3) images were taken at the same time of the year to decrease seasonal effects.

Table 1: Characteristics of SAR data

Date	Time	Incidence angle	Orbit number	Polarization	Centre latitude	Centre longitude
14/01/2007	20:39:35	38.962	5190	HH	2.17695	31.6890
17/07/2007	20:39:40	38.934	7874	HH+HH	2.17933	31.7013
17/10/2007	20:39:17	38.934	9216	HH+HH	2.17369	31.7026
03/06/2008	20:36:18	38.972	12571	HH+HV	2.17599	31.7073
19/07/2008	20:36:17	38.969	13242	HH+HV	2.17928	31.7055
22/10/2009	20:41:24	38.936	19952	HH+HV	2.17682	31.7020
22/01/2010	20:41:19	38.965	21294	HH	2.17636	31.7055
09/03/2010	20:41:04	38.967	21965	HH	2.17663	31.7076
12/03/2011	20:35:48	38.980	27333	HH	2.17351	31.7104

3.2.2. Imagery data preprocessing

In its raw form, the reflected energy from a point target is spread in the range and azimuth directions. Preprocessing is carried out to convert the raw SAR images into single look complex (SLC) images through SAR focusing. The dispersed energy is collected into a single pixel in the output image by carrying out range and azimuth compression (Hanssen, 2001). The resulting images have slant range coordinates, and each pixel is represented using complex numbers to preserve the magnitude and phase information.

3.2.3. SAR processing

SAR images comprise of both the magnitude (energy intensity) and phase difference (time delay) between the transmitted and returned energy which can be represented as single look complex images (SLC). Traditionally, a single SAR image is represented using only the amplitude because the phase of SLC image has no practical value (Mather, 2004). In order to utilize the phase information on SAR data, a minimum of two SLC images are required to compute the phase difference which is useful for estimating the elevation of surface objects and displacement maps. In order to minimize errors arising from processing different polarizations, only the HH polarization was selected for interferometric processing.

Generally, interferometric processing procedure is shown in Figure 2 and involves: co-registration of two SLC images with sufficient coherence (temporal and geometric), generation of interferogram,

computation of coherence, removal of fringe patterns caused by earth curvature (filtering), phase unwrapping, generation of digital elevation models and displacement maps. The exponential notation of a pair of SAR images is represented as indicated in equations 1 and 2,

$$P_1 = a_1 e^{i(\theta_1 + \Phi_1)} \quad (1)$$

$$P_2 = a_2 e^{i(\theta_2 + \Phi_2)} \quad (2)$$

where, P_1 and P_2 are image pixel values, a_1 and a_2 are the amplitudes of the images, Φ_1 and Φ_2 are the deterministic contribution to the phase within the pixel while θ_1 and θ_2 are the random components. An Interferogram (I) shown in equation 3 is generated by performing a complex multiplication of P_2 (slave image) with the conjugate of P_1 (master image). This requires co-registration and resampling of the slave image to the master image. The resulting interferogram contains phase difference ($\Phi 12$) represented using equation 4 which is used to generate 3 D models and surface displacement maps as provided in equation 6.

$$I = a^2 e^{-i\left(\frac{4\pi}{\lambda}(R_1 - R_2)\right)} \quad (3)$$

$$\Phi_{12} = \frac{4\pi}{\lambda}(R_1 - R_2) \quad (4)$$

However, applications of interferometry for surface modelling is dependent on the degree of decorrelation and coherence. A measure of correlation using equation 5, provides the basis for assessing the quality of co-registered images where P1 and P2 are the co- registered images and the asterisks represent the complex conjugate. The correlation values range between 0 (no correlation) and 1 (perfect) correlation between the pair of images.

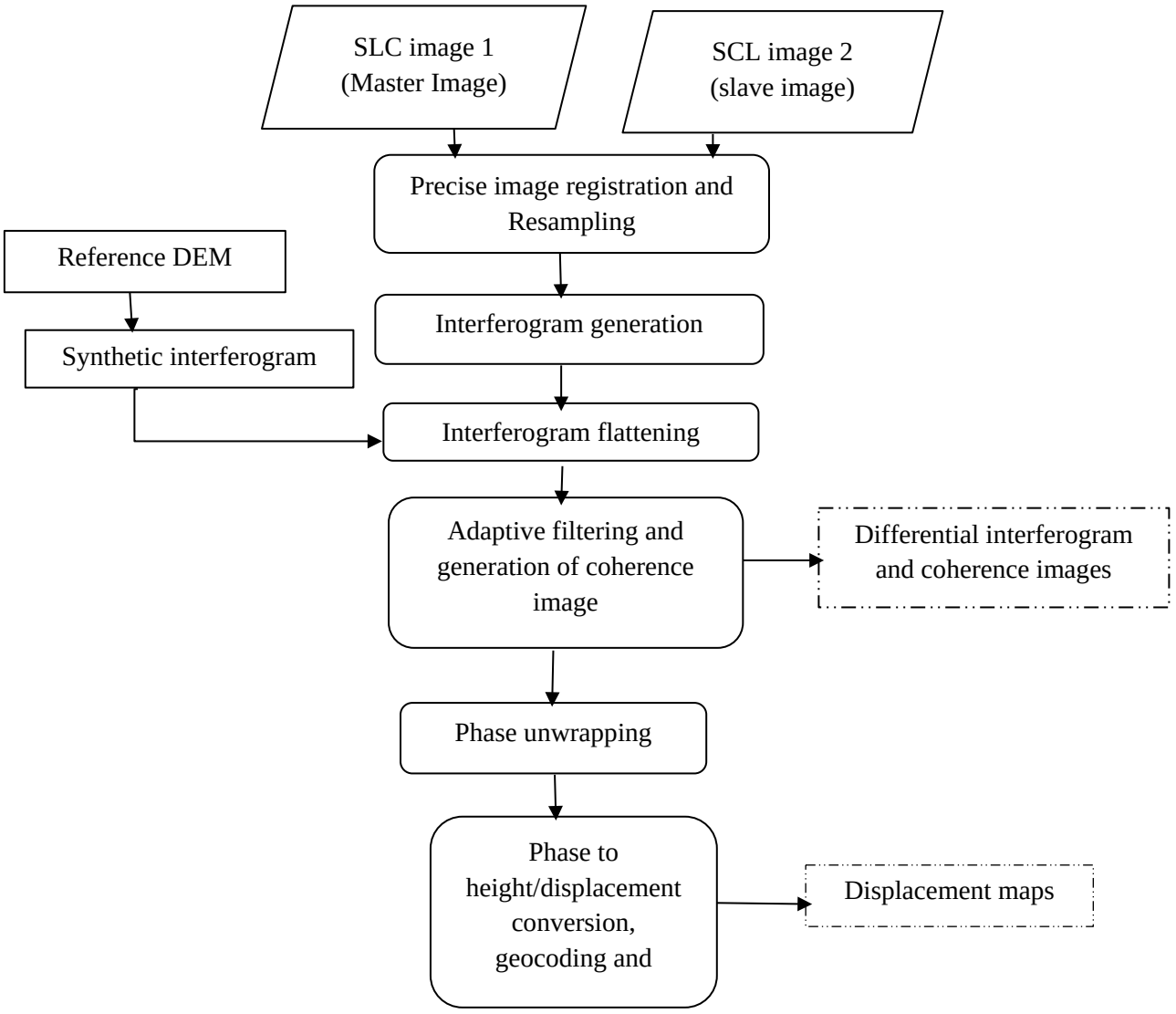

Figure 2: interferometric data processing

$$c = \frac{|\langle P_1 P_2^* \rangle|}{\sqrt{\langle P_1 P_1^* \rangle \langle P_2 P_2^* \rangle}} \quad (5)$$

The interferometric phase in (4) is generally corrupted by noise with a number of components shown in equation 6, where $\Phi_F, \Phi_{T,} \Phi_D, \Phi_P$ and Φ_N are the phase components related to flat earth, topography, coherence displacement, atmospheric path delays and decorrelation noise.

$$\Phi_{12} = \Phi_F + \Phi_T + \Phi_D + \Phi_P + \Phi_N \quad (6)$$

Topography and displacement components are the most important since they are used to generate digital elevation models and displacements maps. Therefore, other phase components are estimated and removed by using reference digital elevation model and filtering. Phase noise is a function of radar system noise, mis-registration and speckle. This is minimized by applying an averaging filter of a given dimension throughout the interferometric phase image. The flat earth phase component is reduced by using reference digital elevation model or three pass differential interferometry. The latter was adopted for the study for two main reasons: 1) 3-pass differential interferometry uses same geometric condition since both topography and deformation pairs have the same master scene (Zebker, Goldstein, Gabriel, & Werner, 1994) 2) it does not require a digital elevation model (DEM).

Three-pass differential interferometry is an approach based on three SAR images to derive two interferograms based on the same reference image. One of the pairs with a short acquisition time interval and rather large interferometric baseline not affected by deformation is used to estimate the topographic phase (Michele Crosetto & Agudo, 2003). The other pair consists of one image before and after the deformation occurs (deformation pair). The flattened interferogram has reduced high frequency phase wrapping caused by imaging geometry. Nevertheless, the wrapped phase will present fringe patterns with discontinuities caused by interferometric phase measurement of only principal value or modulo (2π). A full phase value is determined from the principal value through phase unwrapping and the resulting phase is used to extract elevation values. Phase unwrapping is generally a difficult task but can be made simplified through phase noise reduction and interferometric phase flattening. Interferometric processing was carried out on the SLC images using the SARscape module of Environment for Visualizing Images (ENVI) software.

4. Results and discussion

Figure 3, 4 and 5 show the synthetic digital elevation models, the SAR interferograms and displacement maps for intervals 1, 2, and 3. No continuous fringes were observed in the first interval interferogram, however, a crude pattern of blue to red is observed in the North East of the scene. For intervals two and three, the color ‘fringes’ showing contours of the ground deformation are clearly seen, evidence that ground deformation had taken place. Ground displacement of the whole pixel along range direction translates directly as a phase shift with respect to the rest of the image. The movement along range direction by half a wavelength for the pixel and thus a wavelength of round trip distance for the radar signal creates one fringe. Therefore, one fringe in an interferogram corresponds to the displacement of half the wavelength in the ground displacement in the range direction (Zhou , Chang , & Li 2009).

The number of fringes in the differential interferograms 4b and 4c were counted from a reference point where the surface deformation was supposedly zero. Two major fringes were observed in the center of the study area corresponding to ground deformation of 23.6 cm along the line of sight between the radar and the target for this time interval. A color cycle from yellow-blue-red (YBR) means relative

deformation away from the radar while yellow-red-blue (YRB) suggests relative deformation towards the radar (Hanssen, 2001). From the differential interferogram, a pattern of YRB color is noted in the Northern part of the interferogram.

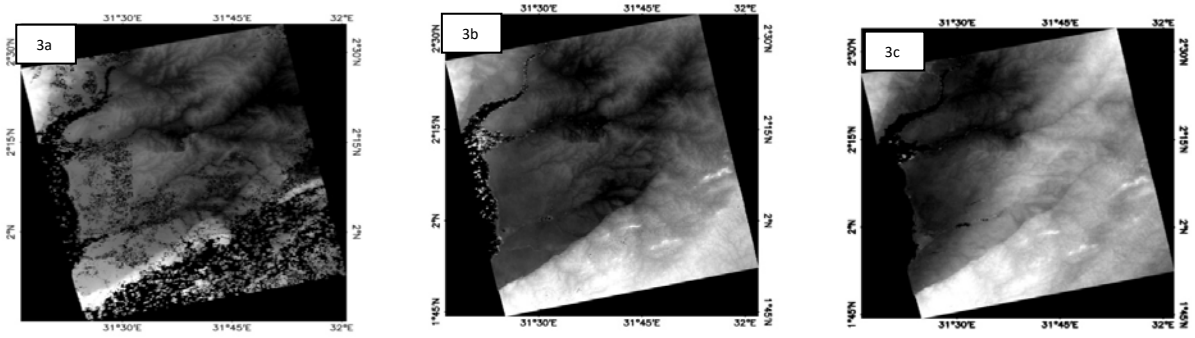

Figure 3: Synthetic Digital elevation models

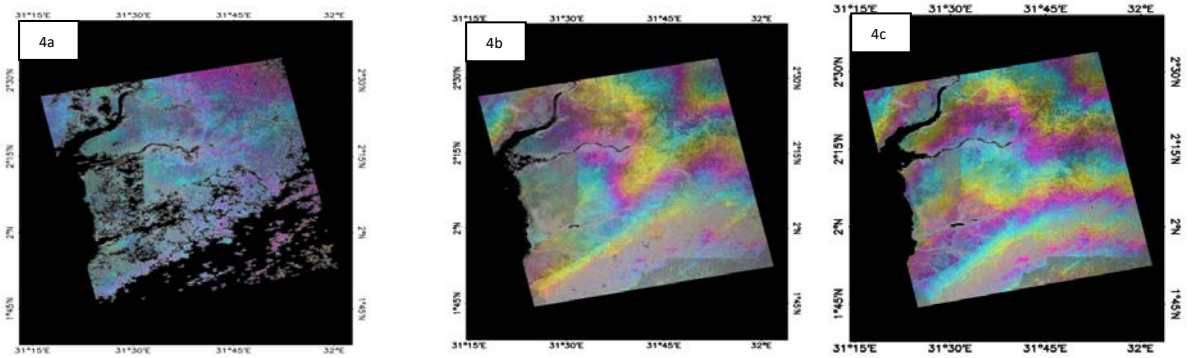

Figure 4: Differential interferograms

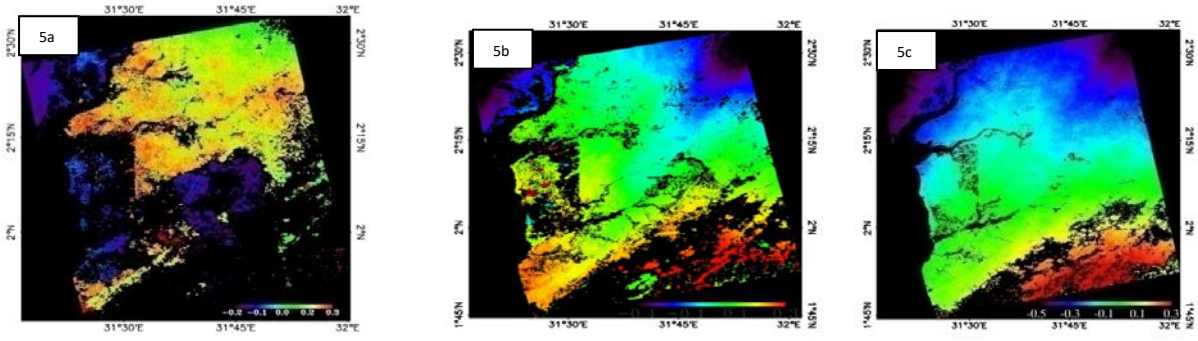

Figure 5: Ground displacement maps

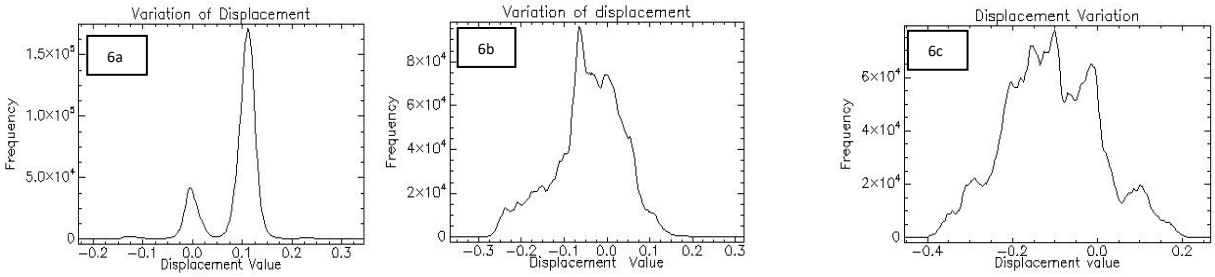

Figure 6: Variation of ground deformation

Patches of decorrelated areas were observed at the southern part of the scene resulting from loss of coherence. The generated differential interferograms were unwrapped and converted to ground displacement images shown in Figure 5 while Figure 6 shows the variation of ground deformation for the three time intervals. It can be observed from the histogram that the estimates of deformation varied between -0.23m to + 0.34m for interval one,–0.37m to +0.32m for interval two, and -0.45m to +0.26m for interval three. The corresponding mean displacements were 0.089 m, -0.04m and –0.10m.

The displacement for interval 1 shows bimodal distribution centered at 0 and 0.1 (approximately the mean value) with low variance. Interval 2 had mean as well as the mode around zero indicating no displacement. However, a number of pixels revealed high positive and negative displacements particularly in north-east, north-west and southern part of the study area. Areas in the north east, northwest and southern part of the study area had high positive displacement values of up to 0.3m indicating high ground movements. Similar observations were made within interval three although with increased variance and magnitude of displacement. The north and north western parts had the highest subsidence levels with a maximum value of -0.45m. A number of factors are attributed to this observed land subsistence and uplift including both anthropogenic and non-anthropogenic activities. However, absence of reliable ground truth seismic data made it difficult to assess the contribution of tectonic activities on the observed deformation. For example, the available seismic data from Ministry of Energy and Mineral Development (MoEMD) did not have same spatial extent with ALOS PALSAR satellite image. Similarly, the data obtained from the United States Geological Survey (USGS) while falling in the study area had years outside the date of ALOS PALSAR data acquisition. However, Google earth Pro platform, Landsat ETM images as well coordinates of existing oil wells were used to investigate the high positive and negative deformation areas as shown in figure 7.

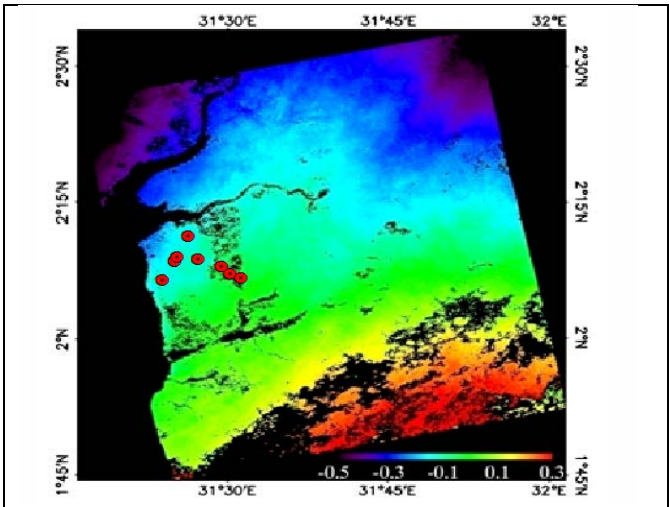

The left image shows the location of some oil wells in the Albertine graben while the right image indicates detail view of Kasemene-1A and Kasemene-2 oil wells on high resolution google image.

Figure 7: Oil well location at Albertine graben

It can be observed that the oil wells of Kasemene1A, Kasemene 2, Wairindi1 and Ngiri 1 were found in areas of high subsidence. This can be attributed to the oil well pad construction that involved cut and fill as well as the spreading and compacting gravel about 300mm thick on the prepared formation ground. The increase in displacement is also associated with drilling activity of the Kigogole 2, Kigogole 4, Kigogole 5 and Nsoga 2 drilling pads.

Visual analysis of Landsat ETM images also indicate an increase in farming activities over the years 2007-2011 within the study area. Agricultural practices have an effect on the interferometric phase leading to ground subsidence and uplift. The low coherence observed in the resulting interferograms can be attributed to changes in land cover and agricultural land use. Despite the lack of validation data for other deformation contributing factors, it is evident that construction of pads and changing land use contributed to the ground deformation of the area. The result also show an overall increase in ground deformation over the given period.

5. Conclusions and Recommendations

The study has demonstrated the application of ALOS PALSAR data for ground deformation assessment in Buliisa oil discovery area. There is a general increase in ground movement over the period 2007-2011 due to oil drilling and agricultural activities. Overall, ground deformation varied between -0.23m and +0.34 for interval one,-0.37m and +0.32m for interval 2, -0.45m and +0.26m for interval three. Low coherence in the generated interferograms led to dark patches that could not be interpreted and hence loss of information in those areas. Lack of ground truth data made it difficult to assess the accuracy of deformation. Future studies should consider a combination of radar interferometric data with data from other geodetic techniques such as GPS to improve understanding of the ground deformation.

6. Acknowledgement

The authors would like to thank Tullow Oil and Council for Frontiers of Knowledge for funding this research for supporting the research. We are also grateful to Japan aerospace exploration agency for providing satellite data used for the study.

7. References

Bakon, M., Papco, J., Perissin, D., Sousa, J. J., & Lazecky, M. (2016). Multi-sensor InSAR Deformation Monitoring over Urban Area of Bratislava (Slovakia). *Procedia Computer Science, 100*(Supplement C), 1127-1134. doi: https://doi.org/10.1016/j.procs.2016.09.265

Barra, A., Monserrat, O., Mazzanti, P., Esposito, C., Crosetto, M., & Scarascia Mugnozza, G. (2016). First insights on the potential of Sentinel-1 for landslides detection. *Geomatics, Natural Hazards and Risk, 7*(6), 1874-1883. doi: 10.1080/19475705.2016.1171258

Braunmüller, P., & Orosz, G. (2012). *The basis of synthetic aperture radar interferometry in Hungary* (Vol. 28).

Bürgmann, R., Rosen, P. A., & Fielding, E. J. (2000). Synthetic Aperture Radar Interferometry to Measure Earth's Surface Topography and Its Deformation. *Annual Review of Earth and Planetary Sciences, 28*(1), 169-209. doi: 10.1146/annurev.earth.28.1.169

Carrasco, D., Alonso, J., & Broquetas, A. (1995, 10-14 Jul1995). *Accuracy assessment of SAR interferometry using the ERS-1*. Paper presented at the Geoscience and Remote Sensing Symposium, 1995. IGARSS '95. 'Quantitative Remote Sensing for Science and Applications', International.

Fujiwara, S., Murakami, M., Nishimura, T., Tobita, M., Yarai, H., & Kobayashi, T. (2017). Volcanic deformation of Atosanupuri volcanic complex in the Kussharo caldera, Japan, from 1993 to 2016 revealed by JERS-1, ALOS, and ALOS-2 radar interferometry. *Earth, Planets and Space, 69*(1), 78. doi: 10.1186/s40623-017-0662-y

Fumiaki, K., Rikio, M., Masayuki, M., Dudy, D., Takeo, I., Yusaku, O., . . . Herri, A. (2004). Ground uplift detected by precise leveling in the Ontake earthquake swarm

area, central Japan in 2002–2004. *Earth Planets Space, 56*.

Gabriel, A. K., Goldstein, R. M., & Zebker, H. A. (1989). Mapping small elevation changes over large areas: Differential radar interferometry. *Journal of Geophysical Research: Solid Earth, 94*(B7), 9183-9191. doi: 10.1029/JB094iB07p09183

Hanssen, R. F. (2001). *Radar Interferomerty,Data Interpretation and Error Analysis*. In F. V. d. Meer (Series Ed.) Remote sensing and Digital Image Processing, Vol. volume 2.

Henderson, F., & Lewis, A. J. (1998). *Principles and Application of Imaging Radar* Vol. 2.

Imamoglu, M., Kahraman, F., Cakir, Z., & Sanli, B. F. (2019). Ground Deformation Analysis of Bolvadin (W. Turkey) by Means of Multi-Temporal InSAR Techniques and Sentinel-1 Data. *Remote Sensing, 11*(9). doi: 10.3390/rs11091069

Jing-xiang, G., & Hong, H. (2009). Advanced GNSS technology of mining deformation monitoring. *Procedia Earth and Planetary Science, 1*(1), 1081-1088. doi: https://doi.org/10.1016/j.proeps.2009.09.166

Jo, M.-J., Jung, H.-S., & Yun, S.-H. (2017). Retrieving Precise Three-Dimensional Deformation on the 2014 M6.0 South Napa Earthquake by Joint Inversion of Multi-Sensor SAR. *Scientific Reports, 7*(1), 5485. doi: 10.1038/s41598-017-06018-0

Kang, Y., Zhao, C., Zhang, Q., Lu, Z., & Li, B. (2017). Application of InSAR Techniques to an Analysis of the Guanling Landslide. *Remote Sensing, 9*(10). doi: 10.3390/rs9101046

Lagios, E., Sakkas, V., Novali, F., Bellotti, F., Ferretti, A., Vlachou, K., & Dietrich, V. (2013). SqueeSAR™ and GPS ground deformation monitoring of Santorini Volcano (1992–2012): Tectonic implications. *Tectonophysics, 594*, 38-59. doi: https://doi.org/10.1016/j.tecto.2013.03.012

Liu, P., Li, Z., Hoey, T., Kincal, C., Zhang, J., Zeng, Q., & Muller, J.-P. (2013). Using advanced InSAR time series techniques to monitor landslide movements in Badong of the Three Gorges region, China. *International Journal of Applied Earth Observation and Geoinformation, 21*(Supplement C), 253-264. doi: https://doi.org/10.1016/j.jag.2011.10.010

Lubitz, C., Motagh, M., & Kaufmann, H. (2014). Ground Surface Response to Geothermal Drilling and the Following Counteractions in Staufen im Breisgau (Germany) Investigated by TerraSAR-X Time Series Analysis and Geophysical Modeling. *Remote Sensing, 6*(11). doi: 10.3390/rs61110571

Maasha, N. (1975). The seismicity and tectonics of Uganda. *Tectonophysics, 27*(4), 381-393. doi: https://doi.org/10.1016/0040-1951(75)90005-0

Massonnet, D., & Feigl, K. (1998). *Massonnet, D. & Feigl, K. L. Radar interferometry and its application to changes in the Earth's surface. Rev. Geophys. 36, 441-500* (Vol. 36).

Massonnet, D., Rossi, M., Carmona, C., Adragna, F., Peltzer, G., Feigl, K., & Rabaute, T. (1993). The displacement field of the Landers earthquake mapped by radar interferometry. *Nature, 364*(6433), 138-142.

Mather, P. M. (2004). *Computer Processing of Remotely-Sensed Images: An Introduction*: Wiley.

Meilano, I., Fumiaki, K., Kazuro, H., Takeshi, S., & Atsushi, Y. (2004). Measuring ground deformations with 1-Hz GPS data: the 2003 Tokachi-oki

earthquake (preliminary report). *Earth Planets Space, 56*.

Michele Crosetto, A. A., Javier Duro, Erlinda Biescas , Marta, & Agudo. (2003). Deformation Monitoring Using Remotely Sensed

Radar Interferometric Data. *Proceedings, 11th FIG Symposium on Deformation Measurements*.

Midzi, V., Hlatywayo, D., Chapola, L., Kebede, F., Atakan, K., K. Lombe, D., . . . Alex Tuhume, F. (1999). *Seismic hazard assessment in Eastern and Southern Africa* (Vol. 42).

Midzi, V., Hlatywayo, D., Chapola, L., Kebede, F., Atakan, K., Lombe, D., Turyomurugyendo, G., & Tugume, F. (1999). Seismic hazard assessment in Eastern and Southern Africa. *Annals of Geophysics, 42*(6). doi: 10.4401/ag-3770

Novellino, A., Cigna, F., Brahmi, M., Sowter, A., Bateson, L., & Marsh, S. (2017). Assessing the Feasibility of a National InSAR Ground Deformation Map of Great Britain with Sentinel-1. *Geosciences, 7*(2), 19.

Ruiz-Armenteros, A. M., Bakon, M., Lazecky, M., Delgado, J. M., Sousa, J. J., Perissin, D., & Caro-Cuenca, M. (2016). Multi-Temporal InSAR Processing Comparison in Presence of High Topography. *Procedia Computer Science, 100*(Supplement C), 1181-1190. doi: https://doi.org/10.1016/j.procs.2016.09.278

Schlögel, R., Doubre, C., Malet, J.-P., & Masson, F. (2015a). Landslide deformation monitoring with ALOS/PALSAR imagery: A D-InSAR geomorphological interpretation method. *Geomorphology, 231*(Supplement C), 314-330. doi: https://doi.org/10.1016/j.geomorph.2014.11.031

Schlögel, R., Doubre, C., Malet, J.-P., & Masson, F. (2015b). Landslide deformation monitoring with ALOS/PALSAR imagery: A D-InSAR geomorphological interpretation method. *Geomorphology, 231*, 314-330. doi: https://doi.org/10.1016/j.geomorph.2014.11.031

Shimada, M. (2010). *On the ALOS/PALSAR operational and interferometric aspects* (Vol. 56).

Shimada, M., & Miyagi, Y. (2009). *Deformation monitoring using the ALOS/PALSAR* (Vol. 2).

Sun, Q., Zhang, L., Ding, X. L., Hu, J., Li, Z. W., & Zhu, J. J. (2015). Slope deformation prior to Zhouqu, China landslide from InSAR time series analysis. *Remote Sensing of Environment, 156*(Supplement C), 45-57. doi: https://doi.org/10.1016/j.rse.2014.09.029

UBOS. (2014). National Population and Housing Census 2014-Main Report. Kampala-Uganda: Uganda Bureau of Statistics.

van Genderen, J. (1996). *SAR Interferometry: Issues, techniqes and applications* (Vol. 17).

Xiaobing , Z., Ni-Bin , C., & Shusun , L. (2009). Applications of SAR Interferometry in Earth and Environmental Science Research. *Sensors, 9*, 1876-1912. doi: 10.3390/s90301876

Zebker, H. A., Goldstein, R. M., Gabriel, A., & Werner, C. L. (1994). On the derivation of coseismic displacement fields using differential radar interferometry. *journal of geophysical Research, 99*, 19617-19634.

Zhang, A., Lu, J., & Kim, J.-W. (2018). Detecting mining-induced ground deformation and associated hazards using spaceborne InSAR techniques. *Geomatics, Natural Hazards and Risk, 9*(1), 211-223. doi: 10.1080/19475705.2017.1415229

Zhou , X., Chang , N.-B., & Li , S. (2009). Applications of SAR interferometry in earth and environmental science research. *Sensors, 9*(3), 1876-1912.